Principles of Small-Molecule Transport through Synthetic Nanopores

Tim Diederichs,[1] Katya Ahmad,[2] Jonathan R. Burns[3], Quoc Hung Nguyen,[4] Zuzanna S. Siwy,[5] Marc Tornow,[4,6,7] Peter V. Coveney,[2,8,*] Robert Tampé,[1,*] Stefan Howorka[3, *]

[1]Institute of Biochemistry, Biocenter, Goethe-University Frankfurt, Frankfurt/M., 60438, Germany

[2]Centre for Computational Science, University College London, London, WC1H0AJ, England, UK

[3]Department of Chemistry, Institute for Structural and Molecular Biology, University College London, London, WC1H0AJ, England, UK

[4]Molecular Electronics, Technical University of Munich, Munich, 80333, Germany

[5]School of Physical Sciences, University of California, Irvine, California 92697, United States

[6]Fraunhofer Research Institution for Microsystems and Solid State Technologies (EMFT), Munich, 80686, Germany

[7]Center of NanoScience (CeNS), Ludwig-Maximilian-University, Munich, 80539, Germany

[8]Informatics Institute, University of Amsterdam, Amsterdam, 1090 GH, The Netherlands

Corresponding Authors

* E-mail: p.v.coveney@ucl.ac.uk, tampe@em.uni-frankfurt.de, s.howorka@ucl.ac.uk

ABSTRACT

Synthetic nanopores made from DNA replicate the key biological processes of transporting molecular cargo across lipid bilayers. Understanding transport across the confined space is of fundamental interest and of relevance to a rational design of pores for biotechnological applications. Here we reveal the transport principles of organic molecules through DNA nanopores by synergistically combining experiments and computer simulations. Using a highly parallel nanostructured platform, we synchronously measure the kinetic flux across hundreds of individual pores to obtain rate constants. The single-channel transport kinetics are close to the theoretical maximum, while selectivity is determined by the interplay of cargo charge and size, the pores' sterics and electrostatics, as well as the embedding lipid bilayer composition. The narrow distribution of transport rates implies a high structural homogeneity of DNA nanopores. The molecular passageway through the nanopore is elucidated *via* coarse-grained constant velocity steered molecular dynamics simulations. The ensemble simulations pinpoint with high resolution and statistical validity the selectivity filter within the lumen and determine the energetic factors governing transport. Our findings on these synthetic pores' structure–function relationship will serve to guide their rational engineering to tailor transport-selectivity for cell biological research, sensing and drug delivery.

Keywords

DNA, nanopore, membrane transport, single-pore analysis, ensemble simulations

ToC graphic

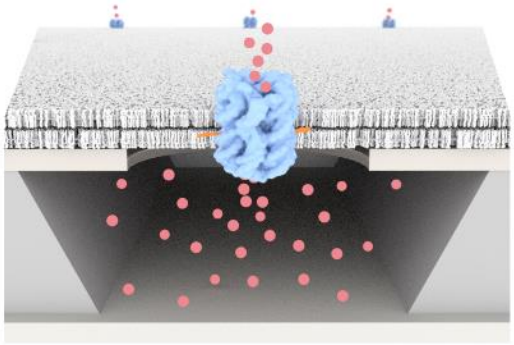

Transport of small molecules across bilayers is essential to support the flow of nutrients into biological cells and to exchange signaling molecules with the environment. Molecular transport across membrane channels is also relevant in synthetic biology to export biotechnologically valuable cargo from engineered host cells. Small-molecule transport through nanopores is, furthermore, the basis for label-free analysis in research and electrical biosensing,[1-14] as prominently epitomized by next-generation fast and portable nanopore sequencing.[13-20] Several molecular entities enable transport, but membrane nanopores are scientifically and technologically the most accessible given their well-known barrel-like structures, the lack of complex conformational rearrangements, and the ease of making atomistic structural changes. Nanopore engineering is required for tailoring their shape and function to applications in synthetic biology, sensing and drug delivery.

Replicating membrane transport with synthetic nanopores is scientifically exciting and can offer step-changes in biotechnological applications. Synthetic nanopores can drastically expand the structural and functional range of membrane nanopores[10,21-25] not accessible with biogenic proteins or peptides, despite considerable progress.[26-29] Among many possible building blocks, DNA[30-42] is the best for creating nanoscale channels given the ease of predicting DNA folding.[43-44] By harnessing DNA nanotechnology, synthetic pores have become available with tuneable inner widths ranging from 0.5 nm to 6 nm.[30-31,36-38,41] As a further benefit, DNA nanopores can be functionally enhanced to open the lumen with physical or biochemical stimuli,[31,45] something which is difficult to rationally design with proteins.

Understanding the transport properties of DNA nanopores is crucial. Insights provide the important scientific link between function and structure, thereby allowing advanced rational design of pores in applications. Furthermore, nanopores composed of negatively charged DNA can serve

as templates for other synthetic hybrid DNA-peptide and solid-state pores of similar charge composition. So far, DNA nanopores have been characterized mostly on their nanoscale architecture and electrical conductance.[32-33,46-47] The translocation of protein and DNA was examined under electric fields[36-37] and by diffusion of selected organic dyes.[31,48] Nevertheless, the knowledge of transport through synthetic channels is limited due to the paucity of studies on small molecules even though this cargo class can offer the richest insight into their molecular interactions with the pore lumen. Small-molecule flux through DNA pores is also relevant for a scientific comparison to protein pores, and for biosensing and drug-delivery applications.

Several fundamental questions are basically unsolved. What are the experimental rates of small molecule transport per channel, particularly under nonbiasing diffusive conditions, and how are the rates influenced by the intrinsic properties of the analytes? Is there any impact of the lipidic environment, and how heterogeneous are the translocation characteristics between different individual pores? Furthermore, what is the molecular path of transport through the pore lumen, and which energetic factors govern the translocation *via* the channel? Finally, how efficient is transport through the synthetic pores in comparison to theoretical calculations and biological protein channels? These questions are unanswered largely due to previous choices of analysis methods which measure either transport of salt ions,[19,49-50] or bulk flurophores that mask properties discernible only at the level of single channels.[31] Similarly, molecular dynamics simulation have so far explored DNA pores[51-52] but not yet obtained insight into dynamic small-molecule transport. Combining experiments and computer simulations, as we do here, is often the best way to obtain a comprehensive picture.

In this report we pioneer a highly synergistic two-pronged experimental and computational approach to reveal the molecular transport principles of synthetic DNA pores with an archetypal

barrel structure.[31] We examine translocation using a massively parallel analysis platform of nanopore-supported membranes (Figure 1a,b) to obtain flux rates of hundreds of individual channels, as well as differently charged and sized small-molecule dyes, ATTO655, 6-carboxyfluorescein (FAM), and Calcein (Figure 1c). The nanostructured platform is ideal to discern static and temporal heterogeneity of molecular transport[53] neither accessible with bulk methods[31] nor with standard low-throughput recordings using salt ions and biasing electric fields.[19,49-50] Our platform singulates nanopores in lipid bilayers suspended over a horizontal array of femtoliter microcavities (Figure 1a) and helps to track diffusive fluorophore transport along a concentration gradient with high temporal and spatial resolution, as demonstrated previously using protein pores.[54-56] The chips with more than 14,000 cavities are ideal for dissecting single-pore kinetics at high-throughput.[37,57] The chip architecture provides sub-nanoscale smooth surfaces and well-defined orifice edges to attain planar supported membranes (Figure 1a) and thereby avoid complicating membrane curvatures.

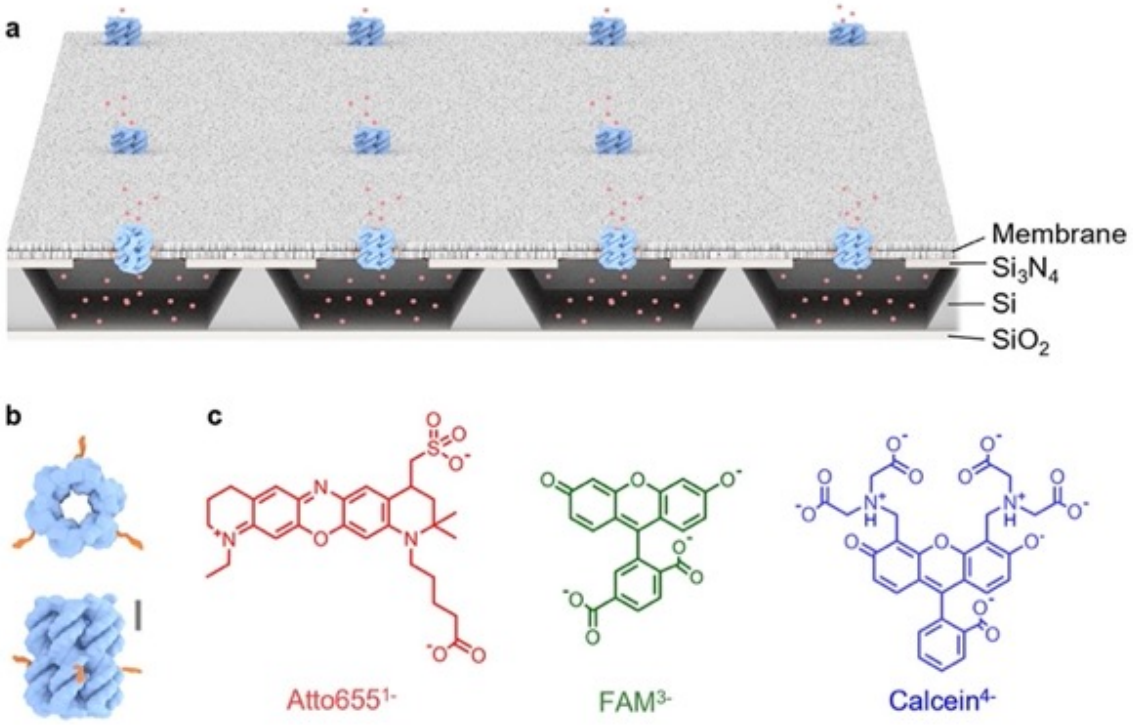

Figure 1. Overview of a microcavity array with supported lipid bilayers used to analyze small molecule transport through DNA nanopores. **a,** Rendering of Si_3N_4/Si/SiO_2-based chip featuring 50 fL microcavity arrays sealed by a lipid membrane (top gray layer). Fluorescent small-molecule analytes (red spheres) flow through individual DNA nanopores (blue) leading to changes in fluorescence emission. The pore contains cholesterol moieties (orange) positioned for membrane anchoring. The dimensions are not drawn to scale, and the number of cavities with pores is overrepresented for clarity. **b,** Top and side view of DNA nanopore (NP) (blue) containing three cholesterol membrane anchors (orange) placed at 120° lateral spacing. **c,** Chemical structure of fluorescent dyes ATTO655, 6-carboxyfluorescein (FAM), and Calcein, with -1, -3, and -4 net charges, respectively.

To obtain insight into pore transport, we also use molecular dynamics (MD) simulations, which describes molecular interactions and movement. MD simulations have been key to understand translocation of cargo through biological protein pores[58-63] and structural dynamics of DNA nanopores.[51-52] To explore the so far uncharted topic of molecular transport in high throughput, coarse-grained (CG) simulations are preferred over all-atom (AA) simulations[64] as the former are faster given the reduction of complexity by the grouping of atoms. With some loss of resolution, the potential energy landscape becomes considerably smoother yet remain transferrable to AA simulations.[65]

To further improve the scientific value of our study into molecular transport through DNA pores, we use ensemble simulations[66-67] and pioneer the combination with coarse-grain simulations. The ensemble method compensates for the often largely divergent individual simulation trajectories which are very sensitive to the initial simulation conditions and become exponentially inaccurate with longer simulation times, leading to unreproducible data. Ensemble simulations are established in fluid dynamics and weather forecasting.[66,68-70] Here, we systematically apply ensemble averaging of at least 16 CG simulation replicas[71] to substantially reduce the error bars on the calculations, making it much easier to perform direct comparisons between theory and experiment.[72]

As a final component in our quest for high-quality insight, we apply the ensemble measurements to constant-velocity steered MD (cv-SMD). This simulation approach overcomes the difficulty of obtaining reliable free-energy landscapes for translocation from standard equilibrium MD simulation. In cv-SMD. a force is applied to the grouped molecular cargo atoms to track their position, orientation, and interactions along the transport pathway while keeping the pore atoms

fixed. In this work, we combine the computational approaches into ensemble-based CG cv-SMD to explore translocation pathways.

Our study characterizes molecular transport through an archetypal DNA nanopore. We pioneer the statistically validated analysis of single-pore dye flux, and establish the influence of dye charge and size, and the surrounding membrane lipids on transport rate and selectivity. The results show the transport efficiency is comparable to protein pores, and illuminates the molecular and energetic pathway of cargo transport across the pore. The scientific insights will help catalyze for future DNA pore designs with engineered selectivity filters.

RESULTS AND DISCUSSION

Structure, formation, and characterization of DNA nanopores. The DNA nanopore (NP) is composed of six DNA duplexes and assembled from six oligonucleotides (Figure 1b).[31] Each duplex folds from two DNA strands, which connects to two neighboring duplexes at their termini *via* interduplex loops. The connectivity deviates from the conventional CaDNAno design,[43-44] where each DNA strand spans multiple duplexes.[73-74] The advantage of the present architecture is its reduced complexity and modularity.[75] Cholesterols are positioned at the 3′ termini of three alternating DNA strands to promote membrane insertion (Figure 1b). The NP has a height of ~ 9.0 nm and an outer and inner channel width of 5.0 and 1.8 nm, respectively (Figure 1b, Supporting Figure 1).[31] To fold the pore, six DNA oligonucleotides each with a length of 50 nt were annealed (Supporting Tables 1 and 2). Complete self-assembly of a reference DNA pore without cholesterol anchors was confirmed by a single peak in size-exclusion chromatography which eluted at 7.8 mL, and a width at half-maximum peak height of 0.8 mL (Figure 2a). Omitting one DNA strand from the assembly mixture resulted in delayed elution at 10.0 mL and a broader peak width of 1.4 mL

(Figure 2a), implying a less compact and less defined structure. Formation of the DNA nanopore with three cholesterol tags was also successful as assessed with gel electrophoretic analysis.[31,75]

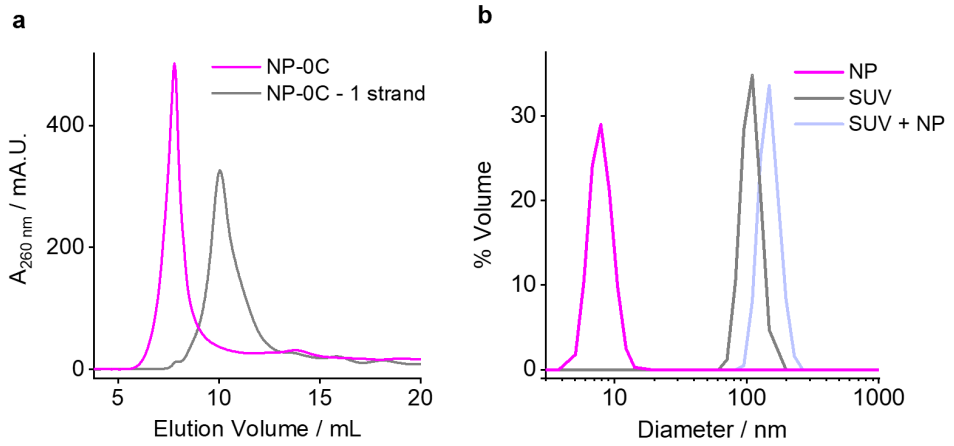

Figure 2. Characterization with size exclusion chromatography and dynamic light scattering confirms DNA nanopore assembly, structure, and membrane interaction. **a**, Size-exclusion chromatography of NP without cholesterol lipid anchors (NP-0C) and the assembly product missing one of the six component DNA strands. **b**, Dynamic light scattering of NP (magenta line), small unilamellar vesicles (SUVs) (gray line), and the two entities combined (light blue line).

NP with three cholesterol tags was analyzed to confirm its interaction with lipid bilayers used in the follow-on transport studies. The pore was incubated with small unilamellar lipid vesicles (SUVs), and membrane incorporation was determined by monitoring changes in vesicle size by dynamic light scattering. SUVs had a diameter of 110 ± 17 nm (mean ± SD, $n = 7$, two independent experiments) (Figure 2b) while incubation with NP led to an increase of the vesicle diameter to 148 ± 26 nm (Figure 2b), implying successful membrane association or pore insertion. In line with expectations, cholesterol-free NP-0C did not lead to a larger SUV diameter (data not shown). NP alone yielded a signal with a diameter of 7.8 ± 2.7 nm (Figure 2b) in agreement with the calculated hydrodynamic diameter of 8.8 nm.

Dye flux through individual DNA nanopores. To analyze the translocation of hundreds of individual membrane-inserted DNA nanopores, we used a high-throughput platform composed of an array of bilayers suspended over fluorophore-filled microcavities (Figure 1a, Figure 3a).[57] The suspended membrane is planar as the microcavities opening is limited to 80 nm diameter in an ultaflat surrounding Si_3N_4 layer. Single DNA nanopores stochastically insert into the small bilayer patch and mediate a diffusive outflow of encapsulated fluorescent probes (Figure 3a) which is trackable by time-lapse fluorescence images of the cavity array (Figure 3b). Consequently, hundreds of individual nanopore transport processes can be visualized in parallel.

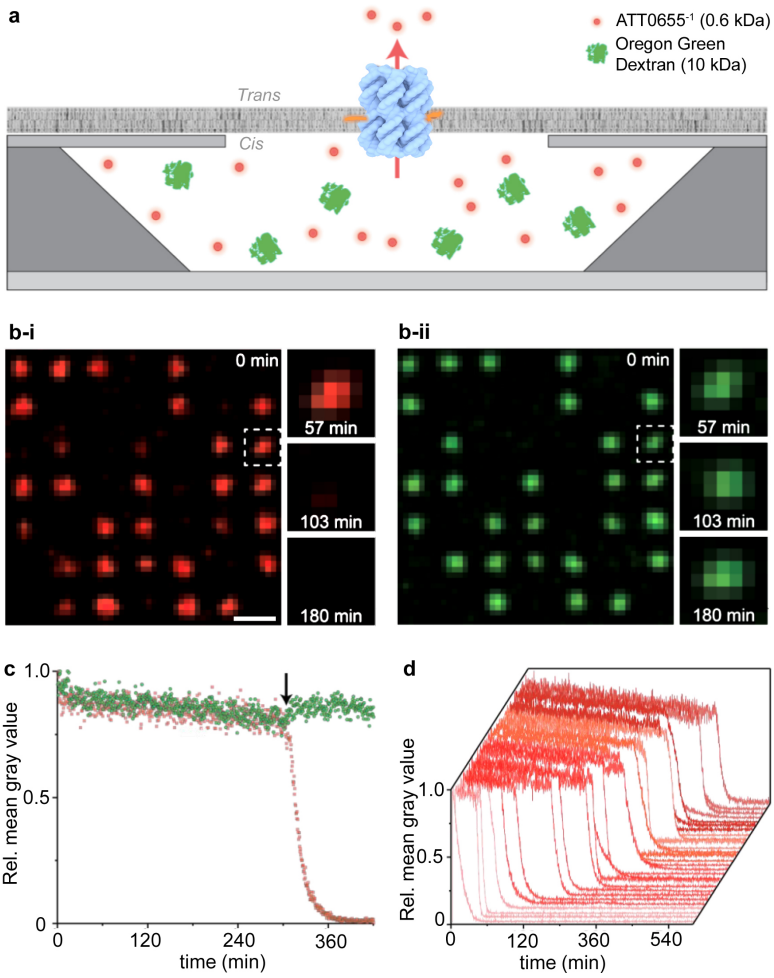

Figure 3. Kinetic analysis of small-molecule transport through DNA nanopores using microcavity arrays. **a,** Illustration of an individual cavity sealed by a solid-supported lipid bilayer with an embedded DNA nanopore. The NP pore permits efflux of the encapsulated ATTO655 (red) but not the larger Oregon Green (OG) Dextran (green). **b,** Confocal laser scanning microscopy images and magnification of microcavities at the stated time points encapsulated with (**b-i**) ATTO655 (red channel) and (**b-ii**) OG Dextran (green channel). Scale bar, 10 µm. **c,** Exemplary normalized fluorescence traces of ATTO655 (red circles) and OG Dextran (green circles) from a single cavity. The arrow denotes the start of the nanopore-mediated transport process. **d,** Multiple normalized ATTO655 efflux traces from individual cavities reveal high flux homogeneity.

We initiated our transport studies using arrays of microcavities filled with ATTO655 (0.6 kDa, 10 μM) and Oregon Green (OG) Dextran (10 kDa, 5 μM) (Figure 3a, b-i, b-ii). ATTO655 with a diffusion-derived hydrodynamic diameter d_h of ~1.2 nm[76] is expected to translocate through the DNA nanopore lumen of 1.8 nm width. By comparison, the control probe OG Dextran, with a d_h of ~3.7 nm[77] cannot permeate NP.

Prior to DNA nanopore addition, the membrane array displayed a homogeneous pattern of fluorescent squares, separated by an expected center-to-center distance of 10 μm reflecting the dimensions of the square-patterned cavity array (Figure 3b). The co-fluorescence signals for both dyes were found for 90% of all microcavities, representing ideal conditions for high-throughput investigations (Supporting Figure 2). Cavities lacking fluorescence are most likely caused by incomplete bilayer formation.

The addition of the DNA nanopore resulted in a significant drop in ATTO655 fluorescence for individual cavities (Figure 3c, red line, final NP concentration of 1.7 nM; Supporting Figure 3a), indicating NP-mediated dye flux from the cavity to the ambient solution. Most efflux traces showed monoexponential fluorescence decays as expected for single-channel transport (Figure 3d). In contrast to flux of small-molecule dye ATTO655, the fluorescence intensity of the control dye OG Dextran remained constant (Figure 3c, green line). The lack of OG Dextran flux also indicates a tight seal between the membrane and the microcavity. A small portion of the cavities showed accidental membrane rupture, resulting in rapid efflux of both fluorescent analytes (Supporting Figure 3b), which was clearly distinguishable from pore-mediated effluxes.

Thousands of individual cavities were subjected to statistical analysis to obtain rate constants for transport through single DNA nanopores. The analysis showed monoexponential NP-mediated

ATTO655 effluxes for 13.7% of the cavities (Figure 4c-i). In further classification, membrane ruptures accounted for 14.3%, unsuitable control with no or weak signals for 3.1%, complex kinetics including two-step decay signals for 5.0%, and no signal changes for 63.9% (Figure 4c-i), similar to other studies using protein-based nanopores.[57] Representative traces for the described categorization are summarized in SI Figure S3. A high ratio of non-fluxing cavities is required to obtain single-pore insertions, as defined by Poisson statistics. The statistical information on NP transport of ATTO655 (Figure 4a-i and b-i) is summarized in a pie chart (Figure 4c-i). A subset of 516 individual fluorescence datasets with a monoexponential ATTO655 decrease and a constant OG Dextran fluorescence was further analyzed to obtain the flux rate. The traces were fitted and the resulting distribution of decay constants, k_{efflux}, was summarized in a histogram (Figure 4d-i).

Efflux traces stemming from individual DNA nanopores were identified by determining the rate distributions for different NP concentrations. High NP concentrations (17 nM) showed a heterogeneous distribution, indicating multiple DNA nanopore insertions per cavity (Supporting Figure 4). By comparison, a 10-fold lower NP concentration revealed four Gaussian distributions with four peaks at $0.44 \pm 0.18 \times 10^{-3}$ s^{-1}, $0.94 \pm 0.21 \times 10^{-3}$ s^{-1}, $1.56 \pm 0.28 \times 10^{-3}$ s^{-1}, and $2.22 \pm 0.44 \times 10^{-3}$ s^{-1} (± SD from the Gaussian fit) most likely representing one, two, three, and four DNA nanopores per cavity (Figure 4d-i). The first peak of the distribution of binned rate values reflects flux through one pore as shown by using a lower concentration of NP of 0.5 nM, which led to a single peak at very comparable value of $0.50 \pm 0.18 \times 10^{-3}$ s^{-1} (Supporting Figure 5). Reducing the nanopore concentration to identify single-pore flux traces is a tested procedure demonstrated previously with other pores.[37,57] The presence of single-pore fluxes is also supported by the monoexponetial decays of efflux traces of single nanopores which showed no leaps or breaks (Figure 3c,d). Without any pores, dye efflux from cavities was only achieved by adding

detergent Triton X-100 to solubilize the membrane or by spontaneous rupture, clearly distinguishable however from pore-mediated effluxes (Supporting Figure 6).

Single-pore transport kinetics depend on cargo charge and size. After establishing that ATTO655 can flux through the NP, we examined transport as a function of cargo charge and size. Therefore, 6-carboxyfluorescein (FAM, 0.4 kDa) with a net charge of -3 and a d_h of approximately 1.1 nm and Calcein (0.6 kDa) with a net charge of -4 and a d_h of ~1.5 nm[78] (Figure 4a-ii and a-iii) were examined. Both dyes were expected to display reduced transport rates due to electrostatic repulsion across the lumen of the negatively charged DNA nanopore (Figure 4b-ii and b-iii). We investigated the transport of FAM by entrapping a solution of 10 μM along with Alexa647 Dextran (10 kDa, 5 μM) in the cavities; the dextran-conjugated dye served as control for bilayer integrity. Time-resolved microscopy tracked the efflux of FAM to yield a transport rate constant for single nanopore effluxes of $0.29 \pm 0.13 \times 10^{-3}$ s^{-1} and for double nanopore effluxes of $0.56 \pm 0.20 \times 10^{-3}$ s^{-1} (150 traces) (Supporting Figure 7), which is slower than the single or the double efflux constant of the reference dye ATTO655 at $0.44 \pm 0.18 \times 10^{-3}$ s^{-1} or $0.94 \pm 0.21 \times 10^{-3}$ s^{-1} (516 traces), and in agreement with the more negatively charged nature of FAM.

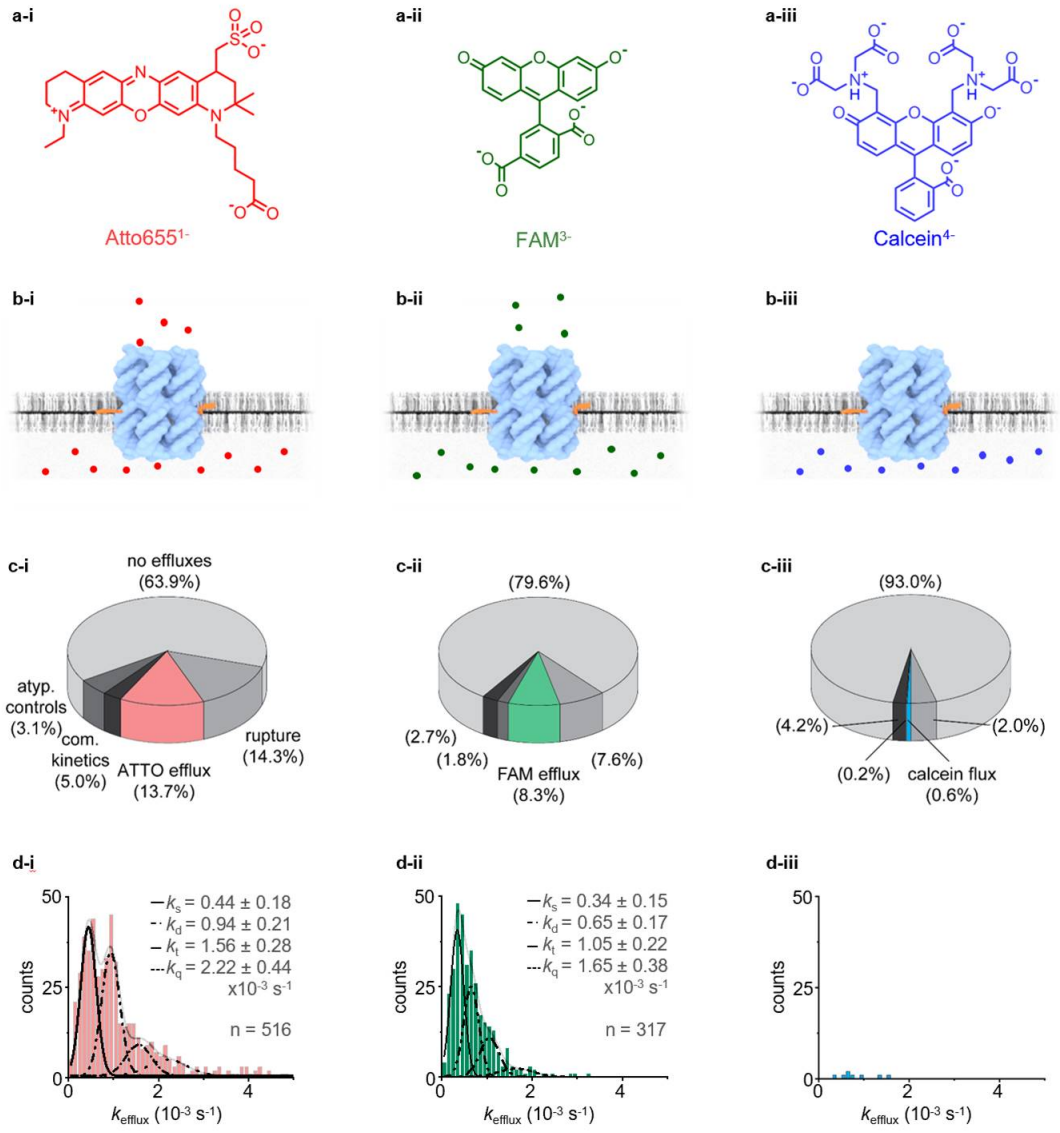

Figure 4. Molecular transport through DNA nanopores depends on cargo charge and size. **a,** Chemical structure of the probe molecules (**a-i**) ATTO655, (**a-ii**) FAM, and (**a-iii**) Calcein. Additional control dyes OG Dextran, ATTO655, and Alexa647 Dextran were co-entrapped in the microcavities for a-I, a-II, and a-III, respectively. **b,** Graphical representation pore transport assays with (**b-i**) ATTO655, (**b-ii**) FAM, and (**b-iii**) Calcein. **c,** Statistics for NP transport (1.7 nM) categorized as NP-mediated efflux, bilayer rupture, atypical controls, complex kinetics, and microcavities without fluorescence changes, shown for (**c-i**) ATTO655 (n = 1,927 traces),

(**c-ii**) FAM (*n* = 4,290 traces), and (**c-iii**) Calcein (*n* = 2,286 traces). **d,** Distribution of NP-mediated effluxes for (**d-i**) ATTO655 (*n* = 327 traces), (**d-ii**) FAM (*n* = 317), and (**d-iii**) Calcein (*n* = 8). Solid and dashed lines indicate Gaussian fits for single and double nanopore efflux constants, respectively.

To confirm the rate constant for FAM, we conducted a co-transport experiment, in which both FAM and ATTO655 were entrapped in the cavities. Analysis of more than 4,000 cavities showed DNA nanopore-mediated efflux in 8.3% of all cases. The other cavities displayed bilayer ruptures (7.6%), complex kinetics (2.7%), unsuitable controls (1.8%), or no signal changes (79.6%) (Figure 4c-ii). Analysis of the monoexponential efflux traces yielded k_{efflux} values, as indicated by single and double Gaussian distributions (Figure 4d-ii). The characteristic k_{efflux} for single DNA nanopore for FAM was $0.34 \pm 0.15 \times 10^{-3}$ s^{-1} (*n* = 317 traces) (Figure 4d-ii), whilst the constant for ATTO655 was $0.48 \pm 0.22 \times 10^{-3}$ s^{-1} (*n* = 327 traces) (Supporting Figure 8). Both values are within the errors obtained for the single-flux experiments. The double, triple, and quadruple nanopore efflux constants for FAM were $0.65 \pm 0.17 \times 10^{-3}$ s^{-1}, $1.05 \pm 0.22 \times 10^{-3}$ s^{-1}, and $1.65 \pm 0.38 \times 10^{-3}$ s^{-1} respectively (Figure 4d-ii). The translocation assay were concluded by adding detergent Triton X-100 to rupture the bilayer leading to the expected rapid non-pore-mediated diffusion of the dyes out of the cavities with similar efflux constants (ATTO655: $24.8 \pm 5.7 \times 10^{-3}$ s^{-1}; FAM: $25.6 \pm 6.8 \times 10^{-3}$ s^{-1}) (Supporting Figure 9).

To further examine the charge and size-selective transport across the DNA nanopores, the flux of Calcein was investigated. The four times negatively charged dye (10 µM) and the control dye Alexa647 Dextran (10 kDa, 5 µM) were entrapped in the cavities (Figure 4b-iii). Quantitative analysis of more than 2,286 traces revealed that only 0.6% of the cavities displayed a NP-like efflux (Figure 4c-iii). This is a more than 20-fold drop in the occurrence compared to the reference

dye ATTO655 and indicates that electrostatics hinder the transport of multiply negatively charged Calcein through NP. Considering how flux for Calcein, FAM, and ATTO655 represents a trend on the influence of cargo charge, we would expect that solely positively charged dyes flux well across the DNA nanopores. Some slow-down due to electrostatic attraction to the negatively charged pore wall cannot be ruled out. Our flux analysis of dyes pioneers kinetic transport rates for single DNA pores, and quantifies how cargo charge and size of small molecule influence the rates.

Flux through the DNA nanopores is influenced by the surrounding lipid bilayer. The transport of the FAM probe through the DNA nanopore has previously been explored with ensemble transport assays.[31] In these experiments, the dye did not pass through the DNA nanopores inserted into small unilamellar vesicles (SUVs) while our current data indicate moderate transport. One difference is that our current study uses flat membranes which are suspended over microcavities, while the past study employed highly curved bilayers which can cause higher lateral pressures on nanopores. Furthermore, the current assay uses membranes containing 30 mol% of negatively charged lipid POPG, while the previous SUV solely contained net neutral lipids including 1,2-dioleoyl-sn-glycero-3-phosphocholine (DOPC). Both curvature and lipid composition are known to influence the shape and function of protein pores[79] and this might also affect the flux properties of our artificial nanopores.

To identify whether curvature or lipid composition influences transport, we conducted transport assays with giant unilamellar vesicles (GUVs) whose membranes' are similarly flat as planar membranes of the microcavity array. The flux was analyzed in GUV with and without 30 mol% POPG. We first examined the negatively charged 1-palmitoyl-2-oleoyl-sn-glycero-3-

phosphoglycerol (POPG)-GUVs containing FAM (10 μM) and control Alexa647 dextran (10 kDa, 3.2 μM) in the surrounding ambient solution. Incubation of GUVs with NP (322 nM) for 2 h led to efflux of FAM (Supporting Figure 10 and 11), thereby confirming pore-mediated dye transport, as found in the microcavity array. Membrane leakiness of GUVs can be ruled out as Alexa647 dextran remained compartmentalized (Supporting Figure 10 and 11). Similarly, bleaching of FAM can be neglected because GUVs showed no NP-mediated efflux (Supporting Figure 11). In further agreement, transport across NP occurred with ATTO655 while control OG dextran (10 kDa) remained compartmentalized (Supporting Figure 12).

Using GUVs without POPG provided a different picture. Here, the inserted DNA nanopores hindered transport of FAM while flux of ATTO655 was facilitated (Supporting Figure 13 and 14). The differential findings on FAM flux with two GUV membrane types strongly suggests that the negatively charged POPG lipid alters the structure of DNA nanopore and hence its transport properties. This striking finding is discussed in the conclusions.

DNA nanopore flux is efficient and comparable to protein pores. To gain insight into the efficiency of pore-mediated transport, we compared the NP flux rate of ATTO655 to the rate for a reference protein pore previously examined with the microcavity array. The efflux constant for individual DNA nanopores of $0.44 \pm 0.18 \times 10^{-3}$ s^{-1} is close to the value of reference pore α-hemolysin (αHL) at $0.96 \pm 0.55 \times 10^{-3}$ s^{-1} (Table 1).[57] After normalizing to account for the differing cross-sectional channel areas, the rate constant for the DNA nanopore is 1.73×10^{4} s^{-1} nm^{-2}. This value is approximately 3.6-fold lower than for the protein pore with a value of 6.23×10^{-4} s^{-1} nm^{-2} (Table 1). Nevertheless, the NP transport rate is relatively high

considering that the net negatively charged ATTO655 dye passes a DNA pore lumen lined with a high density of negative charges (~1 charge nm^{-2}) while the protein channel is less charged.[80]

Using the rate constant for NP, we inferred the single-pore flux *J* to be ~133 ATTO655 fluorophores per second. The value was obtained by determining the total number of fluorophores at an initial concentration of 10 μM inside the cavity volume of 50 fL, and dividing by the rate constant per second. By comparison, the theoretical maximum transport was calculated using equation 1, which integrates previous biophysical models,[81-82] as well as a probability factor to describe the hindrance of solute diffusion within the pore,[79]

$$J = \frac{D\,\Delta c\,\pi\,r^2\,N}{L}\left(1-\frac{a}{r}\right)^2 \qquad (eq.1)$$

where *D* is the diffusion coefficient of the fluorophore in water, Δc the difference in fluorophore concentrations on both sides of the membrane, *r* the pore radius, *N* the Avogadro constant, *L* the pore length, and *a* the solute radius. Due to the tight fit of the analyte in the pore, small variations in radii or length have large effects on the maximal flux. Other complicating factors are the uncertainty of the exact dimensions of the bilayer-embedded NP and the varied orientation of the cylindrical ATTO655 within the lumen. To account for these factors, we assumed a variation of radii and the length by ± 0.1 nm and ± 1 nm, respectively. This yielded a single-pore flux ranging between 16 and 229 molecules per second. Reassuringly, the experimental flux of ~133 dye molecules per second is in the middle of the maximal flux range, highlighting that negatively charged NP effectively transports without an applied electric force.

Another favorable characteristic of the DNA nanopores was revealed when comparing the experimental single-channel rate constants with those of the published protein pore on another measure. In particular, the distribution of rate constant *k* for DNA nanopores was similar to the structurally homogenous protein pore αHL (Table 1). This indicates that synthetic DNA nanopores

have, under the applied experimental conditions, a similar structural homogeneity as the biological protein pore of known atomistic architecture[80] with small dynamic variations.[83]

Table 1: Comparison of DNA nanopores with protein pores in terms of molecular flux and atomistic dimensions[a]

	DNA nanopore	αHL
reference	this study	ref.[57]
rate constant k for flux (s^{-1})[a]	0.44 x 10^{-3}	0.96 x 10^{-3}
cross-sectional area (nm^2)	2.55	1.54
rate constant / cross-sectional area (s^{-1} nm^{-2})	1.73 x 10^{-4}	6.23 x 10^{-4}
width of k distribution (HWHM/mean) (%)[b]	45.8	33.6

[a]Fluxes through all pores were determined using a concentration of 10 μM ATTO655 in the microcavities of the transparent silicon-on-insulator (SOI) chip. [b]HWHM, half-width at half-maximum, and the width is taken for the histogram obtained with 1.7 nM DNA nanopores.

Simulations identify the molecular and energetic pathway for transport. Simulations were carried out to identify the transport pathways of fluorophores through the DNA nanopore and to characterize the associated free energy profiles (potentials of mean force, PMFs). We investigated the fluorophore ATTO655 (Figure 1c) which exhibits high experimental pore flux in this study, and FAM (Figure 1c) of lower transport efficiency.[31] By comparing the PMFs, our aim was to identify the chemical features that enable efficient ATTO665 translocation through the membrane-spanning DNA nanopore, and to thereby explain the experimental flux results. To simulate the translocation of fluorophores through the DNA nanopore lumen, we used ensemble-

based cv-SMD and umbrella sampling. This enhanced method is particularly expedient for characterizing free energy landscapes of molecular translocation, for identifying energetic barriers of transport, and associated chemical and structural features that influence cargo translocation.

Our simulation set-up is shown in Figure 5a and includes the DNA nanopore inserted into a membrane composed of charge-neutral POPC lipids. The structural model was first developed in an all-atom version. An equilibrated confirmation was then converted into the the coarse-grain version. Reflecting their dynamic nature, the pore's DNA duplexes showed flexibility in the simulations. Clustering of the various dynamic structures was performed on an ensemble of equilibrium simulations. The most populous cluster representative of 70% of the conformations was used for the transport simulations (Figure 5a).

cv-SMD simulations were carried out to replicate the experimental flux of efficient and poorly translocating dyes. In the simulations, a pulling force was applied to a dummy atom (Figure 5a, gray sphere) which was harmonically coupled to the fluorophore (Figure 5a, red/green star). The pulling rate in our simulations with a value of 2 nm/ns is within the range of 1 nm/ns to 10 nm/ns used in other studies.[63,84] Reflecting the dynamic nature of nanopore, conformational restraints on the DNA backbone were applied in order to avoid clashes between the fluorophore and the otherwise fluctuating DNA atoms. Pulling the dye across the translocation coordinate (ζ) yielded a trajectory. Snapshot frames seeded separate umbrella sampling simulations, where the fluorophore is restrained within a sampling window using an umbrella biasing potential (Figure 5a, sampling window indicated by dashed lines). The resulting histograms of configurations were force-unbiased by the weighted histogram analysis method (WHAM) to produce a smooth PMF curve describing the one-dimensional free energy profile of the transport process. By using umbrella sampling and WHAM, the non-equillibium cv-SMD simulations generate equilibrium-

like energy profiles. PMFs generated *via* the coarse-grain model generally reflect well the location of free energy peaks and basins but are smoothened compared to the higher-resolution all-atomistic models.

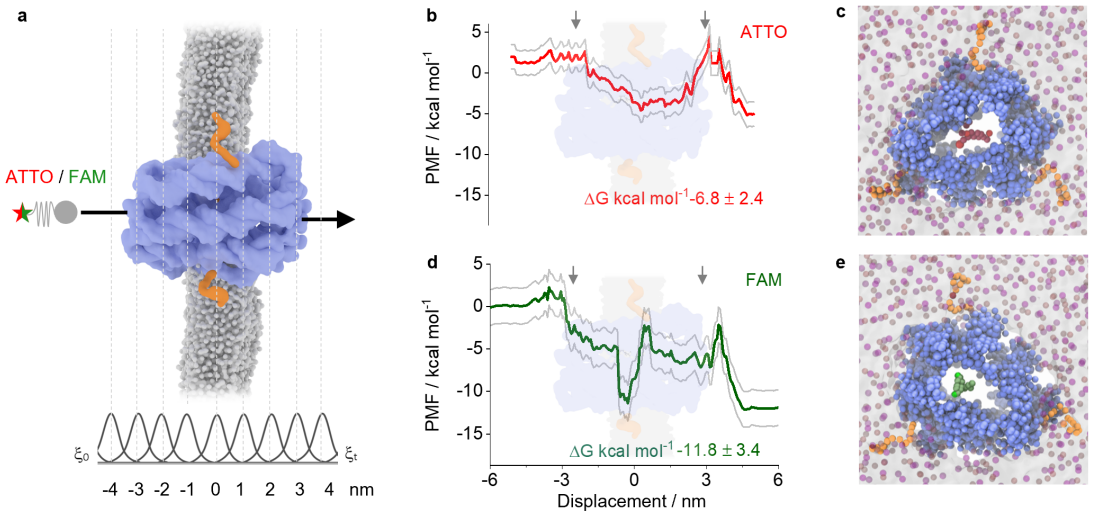

Figure 5. Constant-velocity coarse-grained simulations provide molecular insight into the transport of fluorophores across DNA nanopores. **a,** The computational system used to simulate fluorophore transport. Small-molecule dyes (star, green for FAM, red for ATTO655) are pulled along the translocation coordinate ζ by a dummy atom to which the fluorophore is harmonically coupled (circle). The string represents the harmonic restraint that tethers the fluorophore to the dummy atom. The histograms indicate ensemble configurations that are generated in the umbrella sampling simulations obtained from the cv-SMD simulations. **b,** PMF for the translocation of ATTO655 across the lumen of the DNA nanopore. **c,** Simulation snapshot from the cv-SMD trajectory of the pore translocation of ATTO655. The DNA nanopore is colored blue, its cholesterol units in orange, and the dye's negatively charged sulfate and carboxylate groups in red and its positive part in magenta. Lipid headgroups are in pink and phosphates in purple. An increasing distance in *z*-direction from the viewer is indicated by a grey gradient. **d,** PMF for the

translocation of FAM across the lumen of the DNA nanopore. **e,** Simulation snapshot from the cv-SMD trajectory of the pore translocation of FAM. The dye's three negatively charged moieties are indicated in green. The remaining color coding is the same as in panel (**c**).

The simulations on ATTO655 transport through the DNA nanopore are shown in a movie (Supporting Movies 1 and 2), summarized in a free energy landscape for cargo translocation (Figure 5b), and illustrated by a snapshot (Figure 5c). At the beginning of the transport pathway, ATTO655 aligns its positively charged groups to the negatively charged opposing DNA pore duplexes (Supporting Movies 1 and 2). The associated alignment increases the energetic barrier slightly for entrance into the narrow pore opening by 1.5 kcal mol^{-1} (Figure 5b, left arrow). Upon pore entrance, the dye's negatively charged sulfate and carboxylate groups (Figure 5c, red spheres) maintain a distance of ~ 1.5 nm from the DNA backbone within the approximate 2.5 nm wide nanopore. The dye navigates the more spacious and wider part of the pore lumen without encountering any steric clashes, resulting in the gradual decrease in free energy. The molecule passes the other constriction, causing an increase in free energy of ~ 2.5 kcal mol^{-1} (Figure 5b, right arrow) as the anionic sulfate and carboxylate groups are forced into close contact with the DNA backbone pseudo-atoms (Figure 5c, Supporting Movies 1 and 2). The PMF plots for the entire translocation (Figure 5b) indicate the energy barriers for hindered entrance and departure of the ATTO655 dye into and out of the DNA nanopore and thereby help explain the kinetic transport rate. The PMF's energy difference before pore entrance and after pore exit also yields the Gibbs free energy for translocation with a value of ΔG_{trans} = -6.8 ± 2.4 kcal mol^{-1} (Figure 5b).

For the negatively charged FAM dye, the translocation path (Supporting Movies 3 and 4) shows a different PMF (Figure 5d) than to ATTO655. After pore entrance, there is a sharp free energy

barrier of ~ 15 kcal/mol which coincides with translocates across the pore midsection (Figure 5d). This barrier is found solely for FAM (Figure 5b, ATTO655) and explains the diminished experimental flux of the dye. The energetic barrier stems from the electrostatic repulsion of the negatively charged FAM dye by the negatively charged pore wall, as indicated by the spatial separation of the dye from the wall (Figure 5e). The ΔG_{trans} for FAM was -11.8 ± 3.4 kcal mol^{-1}, which is of higher magnitude than for the ATTO655 dye. The interpretation of ΔG_{trans} has, however, to consider adsorption effects of the dye at the *trans* membrane side, and cannot serve to directly infer the spontaneity of the translocation process. The nonzero value of ΔG_{trans} is also likely due to asymmetric electrostatic environments at the *trans* and *cis* side of the nanopore which reflect the asymmetry in the simulated nanopore and curved membrane, and a polarizable water model. To avoid electrostatic asymmetry, possible future simulations could be conducted with a larger box with more water, and a longer translocation path that avoids contact with the lipid bilayer. Nevertheless, the existing PMFs successfully identify energetic barriers related to the poorer FAM transport found in experiments.

In addition to the *trans*-lumen (TL) translocation, the cv-SMD simulations revealed dye passage *via* an interface (IF) pathway. In this case, both FAM and ATTO655 move at the interface between the pore and surrounding membrane without entering the pore lumen (Supporting Figure 15, Supporting Movies 5 and 6). The IF pathway proceeds *via* dynamically formed gaps between the outer pore perimeter and the surrounding lipid bilayer. The life-time of the gaps is sufficient to permit the fast transport of dyes within the 5 ns-long cv-SMD simulations where the dye is pulled across the pore. The pulling speeds up dye translocation 1000-fold compared to the equilibrium 1D diffusion. Consequently, IF pathway discovered in simulations may not be representative of transport in experiments. Indeed, previous flux data[31] strongly disagree with dye transport *via* the

IF pathway at the time scale relevant in experiments. The previous study used a related six-duplex DNA nanopore but carried a lid that blocks the lumen and hence the translumen pathway. As only minimal dye flux was observed for this blocked pore, it is clear that the IF pathway does not have a major contribution in experiments; the dye flux resumed when the pore was opened. Nevertheless, the cv-SMD simulation highlight the IF pathway which would have remained hidden if examined solely with experiments.

CONCLUSIONS

Our study provides molecular insight into small-molecule transport through synthetic DNA pores. The findings are of fundamental scientific interest and relevance for technological applications. Unlike previous studies on ensemble transport, we present single-channel rate constants for small-molecule flux which is essential to establish fundamental principles for transport through the synthetic pores. We examined the kinetics of charge- and size-selective transport with a high-throughput platform of membrane arrays. Complementing ensemble-based cv-SMD revealed how atomistic and energetic factors shape the transport pathway. Several findings stand out. Firstly, the negatively charged channel lumen exerts a high control over cargo transport as shown by efficient ATTO655 flux but blocking of Calcein transport. The charge and size-dependent control is due to the negatively charged selectivity filter of the DNA nanopore. Our simulations pinpoint the position of the selectivity filter in the midsection of the pore. Yet, other smaller electrostatic/steric barriers are also identified at the pore openings.

Secondly, pore transport is influenced by the surrounding lipids. While a previous study with charge-neutral lipids[31] found no transport for the FAM dye, our current analysis with negatively charged POPG lipids shows that the dye is transported. To account for this observation, POPG is assumed to interact with the DNA nanopore to cause electrostatically repulsion-induced pore

dilation to enable FAM transport. Lipids influencing pore structure and function are common among protein channels,[85] and future studies will elucidate the exact influence of lipids on DNA nanopores.

Thirdly, the high flux for the permeating molecule through the DNA nanopores approaches the theoretically possible maximum. To transport efficiently the net-negatively charged dye has to overcome the electrostatic repulsion to the negatively charged NP wall. The surprisingly high flux is underscored by our simulations which reveal little transport hindrance in the pore center, and support by electrostatic interaction between the negatively charged pore and positive charges on the dye. Finally, the examined NP architecture is of high structural homogeneity. This is inferred from the narrow distribution of rate constants and the high proportion of successful monoexponential flux traces. The DNA nanopore matches biological protein pores, which is surprising and important from the perspective of nano-engineers. In conclusion, this report answers important questions about molecular transport through DNA nanopores and will motivate further research into the design of synthetic nanopores composed of assembled DNA strands that have tunable charge sensitivity for applications in cell biology, sensing, and drug delivery.

METHODS

Material. Native and cholesterol-labeled DNA oligonucleotides were purchased from Integrated DNA Technologies (Coralville, IA, USA) on a 1 μmol scale with HPLC or PAGE purification. 1,2-Diphytanoyl-*sn*-glycero-3-phosphocholine (DPhPC), 1-palitoyl-2-oleoyl-*sn*-glycero-3-phosphocholine (POPC), and 1-palitoyl-2-oleoyl-*sn*-glycero-3-phosphoglycerol (POPG), or 1-palitoyl-2-oleoyl-*sn*-glycero-3-phosphoethanolamine (POPE) were procured from Avanti Polar Lipids (Alabaster, AL, USA, or Hamburg, Germany). Cholesterol was from Sigma-Merck. ATTO655 and 1,2-dioleoyl-*sn*-glycero-3-phosphoethanolamine coupled to ATTO390 (DOPE–ATTO390) were purchased from ATTO-TEC (Siegen, Germany) and Oregon Green (OG) Dextran (10 kDa), Alexa647 Dextran, 6-carboxyfluorescein (FAM), and Calcein were purchased from ThermoFisher Scientific (Darmstadt, Germany). Super low melting agarose (HP45.1) was purchased from Carl Roth (Karlsruhe, Germany). Confocal laser scanning microscopy LSM 880 from Zeiss (Jena, Germany). All other reagents and solvents were purchased from Sigma-Aldrich unless stated.

DNA assembly. NP and NP-0C were assembled using an equimolar mixture of DNA oligonucleotides (1 nmol each, dissolved in buffer A: 300 mM KCl, 15 mM TRIS/HCl pH 8.0; total volume 1 mL). After mixing, the solution was incubated at 95 °C for 2 min and cooled to 4 °C at a rate of 5 °C per minute using a MJ Mini Gradient Thermal Cycler PCR (Bio-Rad, US).

Preparation of small unilamellar vesicles for agarose gels and DLS. A solution of 10 mM DPhPC with 1 mM cholesterol in chloroform (200 μL) was added to an oven-dried round bottom flask (10 mL). The solvent was removed under vacuum using a rotary evaporator for 20 min, after which the thin film was dried under ultra-high vacuum for 3 h. Phosphate buffered saline (1 mL)

was added, and the solution was sonicated for 20-30 min at RT. Small unilamellar vesicles (SUVs) were stored in the fridge and used within 7 days. Shortly before use, the SUV solution was vortexed for 2 s. SUVs were subjected to dynamic light scattering to confirm the vesicles' diameter using a Zetasizer Nano S (Malvern, UK). Data presented are the average of seven scans, repeated two times, and collected at 25 °C after an initial 10 min thermal equilibration period.

Formation of large unilamellar vesciles for optical high-throughput analysis. Liposomes composed of POPC, POPE, and POPG were mixed (40:30:30 mol%) as described.[56] Briefly, the solvent was removed under vacuum using a rotary evaporator for 45 min at 45 °C followed by high vacuum for 30 min. Buffer containing 15 mM TRIS/HCl pH 8.0 and 300 mM KCl was added (final lipid concentration 5 mg/mL) followed by sonication for 2 min. Five freeze thawed cycles were conducted followed by storage at -80 °C. The LUV solution was extruded 21 times through 100 nm polycarbonate membranes at the LiposFast Basic extruder (Avestin, Mannheim, Germany).

Fabrication of transparent bottom nano-orifice cavity arrays. The preparation of the nano-orifice cavity chips has been reported previously.[37,57] Silicon-on-insulator (SOI) chips (13 x 13 mm2) were composed of an undoped silicon (100) handling substrate (380 ± 15 µm), a buried oxide (BOX) layer (100 ± 10 nm), and a silicon (100) device layer (3.0 ± 0.5 µm). Stoichiometric Si_3N_4 (thickness ± 50 nm) was deposited on both sides of the chips by low pressure chemical vapor deposition (LPCVD). The first fabrication steps involved photolithography (Shipley S1818 photoresist) and reactive ion etching (RIE, C_4F_8/O_2 gas mixture, 150 W power, and for 85 s) to pattern an open square (1.8 x 1.8 mm^2) into the Si_3N_4 layer at the center of the chip backside. This pattern served as mask for the subsequent, anisotropic etching of the bulk Si in aqueous potassium hydroxide solution (KOH_{aq}) (20 wt%, 80 °C, 3 h), creating a large truncated pyramidal hole up to

the BOX layer. Then, nano-orifice arrays (120 x 120) with 80 nm orifice diameter and orifice-to-orifice distance of 10 µm (both, in x and y direction) were structured in the front-side Si_3N_4 layer by electron-beam lithography (EBL, e_LiNE system, Raith, Dortmund, Germany) at an acceleration voltage of 30 kV and beam current ~30 pA, using EBL resist AR-P 6200 and developer AR 600 546 (Allresist, Strausberg, Germany), followed by another RIE step with the same parameters. The final anisotropic etching of the chips in KOH_{aq} solution (15 wt%, 50 °C, 3.5 h) created arrays of >14,000 homogenous nano-orifice cavities (~50 fL volume), each having a transparent base and the shape of an inverted pyramid which is truncated at the BOX layer.

Spreading of LUVs on microcavity array and NP insertion. For the formation of suspended bilayers, the SOI chip was directly glued on 8-well sticky slides (ibidi, Planegg/Martinsried, Germany). Ethanol was applied to the chip to wet the cavities followed by buffer exchange (15 mM TRIS/HCl pH 8.0, 300 mM KCl, 5 mM $CaCl_2$). The fluorescent dyes ATTO655 and OG Dextran (10 kDa) were added to a final concentration of 10 µM and 5 µM, respectively. For the charge selective measurements 10 µM of ATTO655, FAM, and Calcein were used with 5 µM of Alexa647 Dextran was used as control dye. The fluorophores were sealed in the microcavities by suspended bilayer formation (1 mg/mL for 1 h). After washing the buffer reservoir, DNA nanopores were added at different concentrations depending on the experiment. Concentrations are given in the description of each experiment.

Light microscopy and data analysis. The fluorescent readout was performed with a confocal laser scanning microscope (CLSM) LSM 880 (AxioObserver from Zeiss, Jena, Germany) equipped with a Plan Apochromat 20x/0.8 M27 air objective. Time-lapse images were recorded in various time intervals for multiple hours. Image analysis to identify fluorescent areas was

performed using ImageJ and freely available plugins. Data correlation and curve fitting of ImageJ datasets with eq. 1

$$f(t) = -F_{min} + F_{min}e^{-k_{\mathrm{eff}}t} + \mathrm{c} \qquad (eq.\,1)$$

were performed with the open source software NanocalcFX (from Nanospot GmbH). Further processing of the rate constants (k_{eff}) including descriptive statistics, peak analysis, and Gaussian fitting were performed with Origin Pro 9.1 (OriginLab). The peak of the Gaussian fitting was given as k_{s} or k_{d} values and the SD of the Gaussian fit as error.

Giant unilamellar vesicle formation. Giant proteoliposomes were produced *via* hydrogel assisted swelling by drying a lipid solution of POPC, POPG, POPE, DOPE–ATTO390 (40:30:29.5:0.5 mol%) or of POPC, POPE, DOPE–ATTO390 (50:49.5:0.5 mol%). Polyvinyl alcohol (PVA) solution 5% (w/w) was dissolved in water and heated to 95 °C, followed by cooling to 38 °C. Subsequently, 200 µL of the PVA solution was spread over a cover slide and dried at 50 °C for 30 min. The premixed lipid solution was distributed on the PVA slide and dried for 2 h under vacuum. After drying, the PVA slide was rehydrated in 15 mM TRIS/HCl pH 8.0, 300 mM KCl, containing 200 mM sucrose and incubated for 30 min before harvesting of GUVs. Encapsulated fluorophores (ATTO655 and FAM, each 10 µM) were additionally supplemented in the swelling buffer depending on the experiment.

DNA nanopore-mediated translocation in giant liposomes. GUVs were added to a precoated glass slide of β-casein (30 min incubation of 0.5 mg/mL). Afterwards, the corresponding control dyes (Alexa647 Dextran and OG Dextran 3.2 µM and 5 µM, respectively) were added to the giant liposome exterior. Subsequently, 322 or 500 nM (final concentration) of the DNA nanopore were

added and images were taken by confocal microscopy before and after 2/10 h incubation. Mean grey value analysis for the were performed by ImageJ (https://imagej.nih.gov/ij/download.html).

Set-up of the computational model. The computational model of the DNA nanopore was developed from an all-atom (AA) version of NP using six strand sequences by building the six hexagonally arranged helices with the Nucleic Acid Builder module in AMBERTools and arranging them at inter-helix distance of ~2 nm using PyMOL.[86] Inter-helix crossovers, cholesterol anchors, and the covalent linkages between the cholesterol anchors and nanopore were set up using PyMOL utilities and parameterized within the CHARMM General Force Field using CGenFF version 3.0.1.[87-90] The nanopore was then solvated in a 35 x 35 x 40 nm TIP3 water box using the VMD *solvate* plugin, with a KCl concentration of 0.3 M using the *autoionize* plugin.[91] The system was then minimized for 10,000 steps (2 fs time-steps) using default parameters to relax the strained bonds and unfavourable interactions inherent of the artificial starting structure. A relaxed barrel configuration of the DNA nanopore was then converted to a MARTINI[65,92-93] coarse-grained (CG) representation using the *martinize-dna.*py[94] script which automatically generates an elastic network of restraints optimized to maintain the base-pairing, general structure, and persistence length of double-stranded β-DNA.

A solvated membrane models was built by inserting the CG nanopore into the center of a pre-equilibrated CG POPC bilayer patch, which was solvated with in a box of polarised MARTINI water molecules with the *insane.py*[95] script. Coarse-grained Na^+ and Cl^- ions were added to set NaCl concentration 1.0 M NaCl. A POPC bilayer was selected to model the lipid bilayer as they are used extensively in electrophysiology experiments, and POPC lipids make up a large proportion of the lipids found in eukaryotic cell membranes. The models consisted of ~ 100,000 pseudo- atoms, with overall cell dimensions of 16 nm x 16 nm x 13 nm. A 16 nm x 16 nm

membrane patch was chosen, as this allowed for enough space between periodic images of the nanopore to avoid self-interactions.

As the MARTINI force-field does not feature standardized parameters for small molecule fluorophores, parameters for the FAM and ATTO655 molecules were derived from AA simulations. Two AA topologies were built for each fluorophore, one with general AMBER force-field (GAFF) parameters, for which partial charges were derived from QM data using the restrained electrostatic potential (RESP) procedure, and one with CHARMM general force field parameters derived using the CGenFF web server *without* prior QM calculation of partial charges. These two sets of force-field parameters were tested to determine the extent to which the choice of initial AA force field influenced the final CG MARTINI parameters. CG parameters were derived with PyCGTool.[96] Once the CG MARTINI fluorophores were built, two fully CG models ready for cv-SMD simulations of the translocation pathways through a membrane-spanning nanopore were assembled – one containing a FAM molecule and the other an ATTO655 molecule.

Constant-velocity SMD simulation parameters. For the cv-SMD translocation simulations described in this work, the umbrella pulling scheme was employed where the centre of mass of the pull group is harmonically restrained to a dummy atom, to which a force is applied in the direction of the translocation. An ensemble of 20 individual cv-SMD were collected for each fluorophore system, employing a spring constant of 500 kJ/mol to maximize sampling of conformational space, thus allowing different translocation paths to be explored. The pulling rate was set to 0.002 nm ps^{-1} over a duration of 5 ns, corresponding to a pulling distance of 10 nm from one pore opening to the other. The force experienced by the harmonic spring at each coordinate along the pulling axis was then outputted during the simulations. Two distinct transport pathways arose for each fluorophore, the trans-lumen (TL) pathways and the interfacial (IF) pathway.

Umbrella sampling simulation parameters. The TL and IF trajectories obtained from cv-SMD simulations on the transport process for FAM and ATTO655 served as a starting point for a subsequent ensemble of umbrella sampling simulations. A total of 52 frames were extracted from each cv-SMD trajectory, representing the incremental progression of the translocation coordinate ξ from the start of the translocation to the end point. These frames define the umbrella sampling "windows" (USWs), from which overlapping histograms of configurations are obtained during the US simulations. The ξ distance between neighbouring USW's was ~0.2 nm in each case. In order to keep the translocating molecule (pull group) centered within each umbrella sampling window, a harmonic restraint with a force constant of with a force constant of 500 kcal $mol^{-1}nm^{-2}$ was applied, to promote overlap between USWs while keeping the molecule centred in its sampling window. This yielded a biased distribution of potential energies for each USW, onto which the weighted histogram analysis method (WHAM) was applied to construct a smooth unbiased free energy profile from the histograms of configurations generated by US.[97]

Supporting Information. The Supporting Information is available free of charge at https://pubs.acs.org/doi/10.1021/acsnano.XXXXXX. DNA nanopore structure and strand sequences, CLSM microcavity arrays demonstrating fluorophore sealing efficiency of nanopores, kinetic analyses of nanopore mediated fluorophore efflux in microcavity experiments, confocal fluorescence analysis of nanopore mediated fluorophore efflux from giant liposomes, computed PMFs for interfacial fluorophore transport through DNA nanopores, supplementary movies of pulling simulations depicting fluorophore transport.

Autor contributions

T.D. performed all high-throughput optical recordings including analysis and interpretation as well as giant liposome studies under supervision and conceptional guidance by R.T. J.R.B. assembled DNA pores, performed SEC, dynamic light scattering analysis, and conducted preliminary throughput flux experiments. J.R.B. and T.D. generated images for main text and supporting information. Q.H.N. and T.D. fabricated the SOI nanopore cavity chips under supervision of M.T. The simulations were carried out by K.A. under supervision of P.C.. S.H. and R.T. initiated, planned, and coordinated the project. T.D., J.R.B., K.A., S.Z., P.V.C., R.T., and S.H. interpreted the data, S.H. and T.D. wrote the manuscript with contributions from all other authors.

Acknowledgments

This research was supported by the BBSRC (BB/M012700/1 and BB/M025373/1 to S.H.), the German Research Foundation (SFB 807, TA 157/12, and GRK 1986 to R.T.), the LOEWE program (DynaMem/A3 to R.T.), and a German-Israeli Project Cooperation (DIP, TO 266/8-1) to M.T. and R.T. The simulation work was performed on ARCHER, the UK's national High Performance Computing service, and Cartesius, hosted by the Dutch national High Performance Computing centre SURFsara. The funding for the computational work was provided by CompBioMed and CompBioMed 2 (http://www.compbiomed.eu, Grant Nos 675451 and 823712), and the UCL Provost.

References

1. Huang, G.; Voet, A.; Maglia, G. Frac Nanopores with Adjustable Diameter Identify the Mass of Opposite-Charge Peptides with 44 Dalton Resolution. *Nat. Commun.* **2019,** *10*, 835.

2. Ouldali, H.; Sarthak, K.; Ensslen, T.; Piguet, F.; Manivet, P.; Pelta, J.; Behrends, J. C.; Aksimentiev, A.; Oukhaled, A. Electrical Recognition of the Twenty Proteinogenic Amino Acids Using an Aerolysin Nanopore. *Nat. Nanotechnol.* **2020,** *38*, 176-181.

3. Cao, C.; Ying, Y. L.; Hu, Z. L.; Liao, D. F.; Tian, H.; Long, Y. T. Discrimination of Oligonucleotides of Different Lengths with a Wild-Type Aerolysin Nanopore. *Nat. Nanotechnol.* **2016,** *11*, 713-718.

4. Thakur, A. K.; Movileanu, L. Real-Time Measurement of Protein-Protein Interactions at Single-Molecule Resolution Using a Biological Nanopore. *Nat. Biotechnol.* **2019,** *37*, 96–101.

5. Galenkamp, N. S.; Biesemans, A.; Maglia, G. Directional Conformer Exchange in Dihydrofolate Reductase Revealed by Single-Molecule Nanopore Recordings. *Nat. Chem.* **2020,** *12*, 481-488.

6. Wang, G.; Wang, L.; Han, Y.; Zhou, S.; Guan, X. Nanopore Stochastic Detection: Diversity, Sensitivity, and Beyond. *Acc. Chem. Res.* **2013,** *46*, 2867-2877.

7. Stoloff, D. H.; Wanunu, M. Recent Trends in Nanopores for Biotechnology. *Curr. Opin. Biotechnol.* **2013,** *24*, 699-704.

8. Reiner, J. E.; Balijepalli, A.; Robertson, J. W. F.; Campbell, J.; Suehle, J.; Kasianowicz, J. J. Disease Detection and Management *via* Single Nanopore-Based Sensors. *Chem. Rev.* **2012,** *112*, 6431-6451.

9. Miles, B. N.; Ivanov, A. P.; Wilson, K. A.; Dogan, F.; Japrung, D.; Edel, J. B. Single Molecule Sensing with Solid-State Nanopores: Novel Materials, Methods, and Applications. *Chem. Soc. Rev.* **2013,** *42*, 15-28.

10. Howorka, S. Building Membrane Nanopores. *Nat. Nanotechnol.* **2017,** *12*, 619-630.

11. Restrepo-Perez, L.; Joo, C.; Dekker, C. Paving the Way to Single-Molecule Protein Sequencing. *Nat. Nanotechnol.* **2018,** *13*, 786-796.

12. Zeng, S.; Wen, C.; Solomon, P.; Zhang, S. L.; Zhang, Z. Rectification of Protein Translocation in Truncated Pyramidal Nanopores. *Nat. Nanotechnol.* **2019,** *14*, 1056-1062.

13. Rivas, F.; Zahid, O. K.; Reesink, H. L.; Peal, B. T.; Nixon, A. J.; DeAngelis, P. L.; Skardal, A.; Rahbar, E.; Hall, A. R. Label-Free Analysis of Physiological Hyaluronan Size Distribution with a Solid-State Nanopore Sensor. *Nat. Commun.* **2018,** *9*, 1037.

14. Liu, X.; Mihovilovic Skanata, M.; Stein, D. Entropic Cages for Trapping DNA near a Nanopore. *Nat. Commun.* **2015,** *6*, 6222.

15. Clarke, J.; Wu, H. C.; Jayasinghe, L.; Patel, A.; Reid, S.; Bayley, H. Continuous Base Identification for Single-Molecule Nanopore DNA Sequencing. *Nat. Nanotechnol.* **2009,** *4*, 265-270.

16. Quick, J.; Loman, N. J.; Duraffour, S.; Simpson, J. T.; Severi, E.; Cowley, L.; Bore, J. A.; Koundouno, R.; Dudas, G.; Mikhail, A.; Ouedraogo, N.; Afrough, B.; Bah, A.; Baum, J. H.; Becker-Ziaja, B.; Boettcher, J. P.; Cabeza-Cabrerizo, M.; Camino-Sanchez, A.; Carter, L. L.; Doerrbecker, J., *et al*. Real-Time, Portable Genome Sequencing for Ebola Surveillance. *Nature* **2016,** *530*, 228-232.

17. Jain, M.; Koren, S.; Miga, K. H.; Quick, J.; Rand, A. C.; Sasani, T. A.; Tyson, J. R.; Beggs, A. D.; Dilthey, A. T.; Fiddes, I. T.; Malla, S.; Marriott, H.; Nieto, T.; O'Grady, J.; Olsen, H. E.; Pedersen, B. S.; Rhie, A.; Richardson, H.; Quinlan, A. R.; Snutch, T. P., *et al*. Nanopore Sequencing and Assembly of a Human Genome with Ultra-Long Reads. *Nat. Biotechnol*. **2018,** *36*, 338-345.

18. Van der Verren, S. E.; Van Gerven, N.; Jonckheere, W.; Hambley, R.; Singh, P.; Kilgour, J.; Jordan, M.; Wallace, E. J.; Jayasinghe, L.; Remaut, H. A Dual-Constriction Biological Nanopore Resolves Homonucleotide Sequences with High Fidelity. *Nat. Biotechnol*. **2020,** *38*, 1415–1420.

19. Goyal, P.; Krasteva, P. V.; Van Gerven, N.; Gubellini, F.; Van den Broeck, I.; Troupiotis-Tsaïlaki, A.; Jonckheere, W.; Péhau-Arnaudet, G.; Pinkner, J. S.; Chapman, M. R.; Hultgren, S. J.; Howorka, S.; Fronzes, R.; Remaut, H. Structural and Mechanistic Insights into the Bacterial Amyloid Secretion Channel CsgG. *Nature* **2014,** *516*, 250-253.

20. Wei, R. S.; Gatterdam, V.; Wieneke, R.; Tampe, R.; Rant, U. Stochastic Sensing of Proteins with Receptor-Modified Solid-State Nanopores. *Nat. Nanotechnol*. **2012,** *7*, 257-263.

21. Litvinchuk, S.; Tanaka, H.; Miyatake, T.; Pasini, D.; Tanaka, T.; Bollot, G.; Mareda, J.; Matile, S. Synthetic Pores with Reactive Signal Amplifiers as Artificial Tongues. *Nat. Mater*. **2007,** *6*, 576-580.

22. Vargas Jentzsch, A.; Hennig, A.; Mareda, J.; Matile, S. Synthetic Ion Transporters That Work with Anion-Pi Interactions, Halogen Bonds, and Anion-Macrodipole Interactions. *Acc. Chem. Res*. **2013,** *46*, 2791-2800.

23. Gokel, G. W.; Negin, S. Synthetic Ion Channels: From Pores to Biological Applications. *Acc. Chem. Res.* **2013,** *46*, 2824-2833.

24. Montenegro, J.; Ghadiri, M. R.; Granja, J. R. Ion Channel Models Based on Self-Assembling Cyclic Peptide Nanotubes. *Acc. Chem. Res.* **2013,** *46*, 2955-2965.

25. Zhao, Y.; Cho, H.; Widanapathirana, L.; Zhang, S. Conformationally Controlled Oligocholate Membrane Transporters: Learning through Water Play. *Acc. Chem. Res.* **2013,** *46*, 2763-2772.

26. Xu, C.; Lu, P.; Gamal El-Din, T. M.; Pei, X. Y.; Johnson, M. C.; Uyeda, A.; Bick, M. J.; Xu, Q.; Jiang, D.; Bai, H.; Reggiano, G.; Hsia, Y.; Brunette, T. J.; Dou, J.; Ma, D.; Lynch, E. M.; Boyken, S. E.; Huang, P. S.; Stewart, L.; DiMaio, F., *et al*. Computational Design of Transmembrane Pores. *Nature* **2020,** *585*, 129-134.

27. Mahendran, K. R.; Niitsu, A.; Kong, L.; Thomson, A. R.; Sessions, R. B.; Woolfson, D. N.; Bayley, H. A Monodisperse Transmembrane Alpha-Helical Peptide Barrel. *Nat. Chem.* **2017,** *9*, 411-419.

28. Joh, N. H.; Wang, T.; Bhate, M. P.; Acharya, R.; Wu, Y.; Grabe, M.; Hong, M.; Grigoryan, G.; DeGrado, W. F. De Novo Design of a Transmembrane Zn(2)(+)-Transporting Four-Helix Bundle. *Science* **2014,** *346*, 1520-1524.

29. Lu, P.; Min, D.; DiMaio, F.; Wei, K. Y.; Vahey, M. D.; Boyken, S. E.; Chen, Z.; Fallas, J. A.; Ueda, G.; Sheffler, W.; Mulligan, V. K.; Xu, W.; Bowie, J. U.; Baker, D. Accurate Computational Design of Multipass Transmembrane Proteins. *Science* **2018,** *359*, 1042-1046.

30. Langecker, M.; Arnaut, V.; Martin, T. G.; List, J.; Renner, S.; Mayer, M.; Dietz, H.; Simmel, F. C. Synthetic Lipid Membrane Channels Formed by Designed DNA Nanostructures. *Science* **2012,** *338*, 932-936.

31. Burns, J. R.; Seifert, A.; Fertig, N.; Howorka, S. A Biomimetic DNA-Based Channel for the Ligand-Controlled Transport of Charged Molecular Cargo across a Biological Membrane. *Nat. Nanotechnol.* **2016,** *11*, 152-156.

32. Burns, J.; Stulz, E.; Howorka, S. Self-Assembled DNA Nanopores That Span Lipid Bilayers. *Nano Lett.* **2013,** *13*, 2351-2356.

33. Seifert, A.; Göpfrich, K.; Burns, J. R.; Fertig, N.; Keyser, U. F.; Howorka, S. Bilayer-Spanning DNA Nanopores with Voltage-Switching between Open and Closed State. *ACS Nano* **2015,** *9*, 1117-1126.

34. Chen, L.; Liang, S.; Chen, Y.; Wu, M.; Zhang, Y. Destructing the Plasma Membrane with Activatable Vesicular DNA Nanopores. *ACS Appl. Mater. Interfaces* **2020,** *12*, 96-105.

35. Gopfrich, K.; Li, C. Y.; Ricci, M.; Bhamidimarri, S. P.; Yoo, J.; Gyenes, B.; Ohmann, A.; Winterhalter, M.; Aksimentiev, A.; Keyser, U. F. Large-Conductance Transmembrane Porin Made from DNA Origami. *ACS Nano* **2016,** *10*, 8207-8214.

36. Krishnan, S.; Ziegler, D.; Arnaut, V.; Martin, T. G.; Kapsner, K.; Henneberg, K.; Bausch, A. R.; Dietz, H.; Simmel, F. C. Molecular Transport through Large-Diameter DNA Nanopores. *Nat. Commun.* **2016,** *7*, 12787.

37. Diederichs, T.; Pugh, G.; Dorey, A.; Xing, Y.; Burns, J. R.; Nguyen, Q. H.; Tornow, M.; Tampé, R.; Howorka, S. Synthetic Protein-Conductive Membrane Nanopores Built with DNA. *Nat. Commun.* **2019,** *10*, 5018.

38. Thomsen, R. P.; Malle, M. G.; Okholm, A. H.; Krishnan, S.; Bohr, S. S.; Sorensen, R. S.; Ries, O.; Vogel, S.; Simmel, F. C.; Hatzakis, N. S.; Kjems, J. A Large Size-Selective DNA Nanopore with Sensing Applications. *Nat. Commun.* **2019,** *10*, 5655.

39. Chidchob, P.; Offenbartl-Stiegert, D.; McCarthy, D.; Luo, X.; Li, J. N.; Howorka, S.; Sleiman, H. F. Spatial Presentation of Cholesterol Units on a DNA Cube as a Determinant of Membrane Protein-Mimicking Functions. *J. Am. Chem. Soc.* **2019,** *141*, 1100-1108.

40. Howorka, S. Nanotechnology. Changing of the Guard. *Science* **2016,** *352*, 890-891.

41. Gopfrich, K.; Zettl, T.; Meijering, A. E.; Hernandez-Ainsa, S.; Kocabey, S.; Liedl, T.; Keyser, U. F. DNA-Tile Structures Induce Ionic Currents through Lipid Membranes. *Nano Lett.* **2015,** *15*, 3134-3138.

42. Zhang, Z.; Yang, Y.; Pincet, F.; Llaguno, M.; Lin, C. Placing and Shaping Liposomes with Reconfigurable DNA Nanocages. *Nat. Chem.* **2017,** *9*, 653-659.

43. Douglas, S. M.; Dietz, H.; Liedl, T.; Hogberg, B.; Graf, F.; Shih, W. M. Self-Assembly of DNA into Nanoscale Three-Dimensional Shapes. *Nature* **2009,** *459*, 414-418.

44. Douglas, S. M.; Marblestone, A. H.; Teerapittayanon, S.; Vazquez, A.; Church, G. M.; Shih, W. M. Rapid Prototyping of 3D DNA-Origami Shapes with Cadnano. *Nucleic Acids Res.* **2009,** *37*, 5001-5006.

45. Arnott, P. M.; Howorka, S. A Temperature-Gated Nanovalve Self-Assembled from DNA to Control Molecular Transport across Membranes. *ACS Nano* **2019,** *13*, 3334–3340.

46. Burns, J. R.; Al-Juffali, N.; Janes, S. M.; Howorka, S. Membrane-Spanning DNA Nanopores with Cytotoxic Effect. *Angew. Chem. Int. Ed.* **2014,** *53*, 12466-12470.

47. Burns, J. R.; Göpfrich, K.; Wood, J. W.; Thacker, V. V.; Stulz, E.; Keyser, U. F.; Howorka, S. Lipid Bilayer-Spanning DNA Nanopores with a Bifunctional Porphyrin Anchor. *Angew. Chem. Int. Ed.* **2013,** *52*, 12069–12072.

48. Lanphere, C.; Arnott, P. M.; Jones, S. F.; Korlova, K.; Howorka, S. A Biomimetic DNA-Based Membrane Gate for Protein-Controlled Transport of Cytotoxic Drugs. *Angew. Chem. Int. Ed.* **2021,** *60*, 1903-1908.

49. Del Rio Martinez, J. M.; Zaitseva, E.; Petersen, S.; Baaken, G.; Behrends, J. C. Automated Formation of Lipid Membrane Microarrays for Ionic Single-Molecule Sensing with Protein Nanopores. *Small* **2015,** *11*, 119-125.

50. Davenport, M.; Rodriguez, A.; Shea, K. J.; Siwy, Z. S. Squeezing Ionic Liquids through Nanopores. *Nano Lett.* **2009,** *9*, 2125-2128.

51. Maingi, V.; Burns, J. R.; Uusitalo, J. J.; Howorka, S.; Marrink, S. J.; Sansom, M. S. Stability and Dynamics of Membrane-Spanning DNA Nanopores. *Nat. Commun.* **2017,** *8*, 14784.

52. Maingi, V.; Lelimousin, M.; Howorka, S.; Sansom, M. S. Gating-Like Motions and Wall Porosity in a DNA Nanopore Scaffold Revealed by Molecular Simulations. *ACS Nano* **2015,** *9*, 11209-11217.

53. Zlatanova, J.; van Holde, K. Single-Molecule Biology: What Is It and How Does It Work? *Mol Cell* **2006,** *24*, 317-329.

54. Urban, M.; Kleefen, A.; Mukherjee, N.; Seelheim, P.; Windschiegl, B.; Vor der Bruggen, M.; Kocer, A.; Tampe, R. Highly Parallel Transport Recordings on a Membrane-on-Nanopore Chip at Single Molecule Resolution. *Nano Lett*. **2014,** *14*, 1674-1680.

55. Kusters, I.; van Oijen, A. M.; Driessen, A. J. Membrane-on-a-Chip: Microstructured Silicon/Silicon-Dioxide Chips for High-Throughput Screening of Membrane Transport and Viral Membrane Fusion. *ACS Nano* **2014,** *8*, 3380-3392.

56. Kleefen, A.; Pedone, D.; Grunwald, C.; Wei, R.; Firnkes, M.; Abstreiter, G.; Rant, U.; Tampe, R. Multiplexed Parallel Single Transport Recordings on Nanopore Arrays. *Nano Lett*. **2010,** *10*, 5080–5087.

57. Diederichs, T.; Nguyen, Q. H.; Urban, M.; Tampe, R.; Tornow, M. Transparent Nanopore Cavity Arrays Enable Highly Parallelized Optical Studies of Single Membrane Proteins on Chip. *Nano Lett*. **2018,** *18*, 3901-3910.

58. Herce, H. D.; Garcia, A. E. Molecular Dynamics Simulations Suggest a Mechanism for Translocation of the HIV-1 TAT Peptide across Lipid Membranes. *Proc. Natl. Acad. Sci. U S A* **2007,** *104*, 20805-20810.

59. Mathe, J.; Aksimentiev, A.; Nelson, D. R.; Schulten, K.; Meller, A. Orientation Discrimination of Single-Stranded DNA inside the Alpha-Hemolysin Membrane Channel. *Proc. Natl. Acad. Sci. U S A* **2005,** *102*, 12377-12382.

60. Wells, D. B.; Abramkina, V.; Aksimentiev, A. Exploring Transmembrane Transport through Alpha-Hemolysin with Grid-Steered Molecular Dynamics. *J. Chem. Phys.* **2007,** *127*, 125101.

61. Bond, P. J.; Guy, A. T.; Heron, A. J.; Bayley, H.; Khalid, S. Molecular Dynamics Simulations of DNA within a Nanopore: Arginine-Phosphate Tethering and a Binding/Sliding Mechanism for Translocation. *Biochemistry* **2011,** *50*, 3777-3783.

62. Martin, H.; Jha, S.; Howorka, S.; Coveney, P. Determination of Free Energy Profiles for the Translocation of Polynucleotides through A-Hemolysin Nanopores Using Non-Equilibrium Molecular Dynamics Simulations. *J. Chem. Theory Comput.* **2009,** *5*, 1955-2192.

63. Martin, H. S.; Jha, S.; Coveney, P. V. Comparative Analysis of Nucleotide Translocation through Protein Nanopores Using Steered Molecular Dynamics and an Adaptive Biasing Force. *J. Comput. Chem.* **2014,** *35*, 692-702.

64. Muthukumar, M.; Kong, C. Y. Simulation of Polymer Translocation through Protein Channels. *Proc. Natl. Acad. Sci. U S A* **2006,** *103*, 5273-5278.

65. Marrink, S. J.; Risselada, H. J.; Yefimov, S.; Tieleman, D. P.; de Vries, A. H. The Martini Force Field: Coarse Grained Model for Biomolecular Simulations. *J. Phys. Chem. B* **2007,** *111*, 7812-7824.

66. Coveney, P. V.; Wan, S. On the Calculation of Equilibrium Thermodynamic Properties from Molecular Dynamics. *Phys. Chem. Chem. Phys.* **2016,** *18*, 30236-30240.

67. Wan, S.; Bhati, A. P.; Zasada, S. J.; Coveney, P. V. Rapid, Accurate, Precise and Reproducible Ligand-Protein Binding Free Energy Prediction. *Interface Focus* **2020,** *10*, 20200007.

68. Parliament, U. The Disclosure of Climate Data from the Climatic Research Unit at the University of East Anglia - Science and Technology Committee. https://publications.parliament.uk/pa/cm200910/cmselect/cmsctech/387/38703.htm (accessed July 7, 2021)

69. Palmer, T. The ECMWF Ensemble Prediction System: Looking Back (More Than) 25 Years and Projecting Forward 25 Years. *Q. J. R. Meteorol. Soc.* **2018,** *145*, 12-24.

70. Frisch, U. U. *Turbulence: The Legacy of A.N. Kolmogorov*. Cambridge University Press: New York, 1995.

71. Wan, S.; Knapp, B.; Wright, D. W.; Deane, C. M.; Coveney, P. V. Rapid, Precise, and Reproducible Prediction of Peptide-Mhc Binding Affinities from Molecular Dynamics That Correlate Well with Experiment. *J. Chem. Theory Comput.* **2015,** *11*, 3346-3356.

72. Wan, S.; Sinclair, R. C.; Coveney, P. V. Uncertainty Quantification in Classical Molecular Dynamics. *Philos. Transact. Ser. A Math. Phys. Eng. Sci.* **2020,** *in press*.

73. Yin, P.; Hariadi, R. F.; Sahu, S.; Choi, H. M.; Park, S. H.; Labean, T. H.; Reif, J. H. Programming DNA Tube Circumferences. *Science* **2008,** *321*, 824-826.

74. Wang, T.; Schiffels, D.; Cuesta, S. M.; Fygenson, D. K.; Seeman, N. C. Design and Characterization of 1D Nanotubes and 2D Periodic Arrays Self-Assembled from DNA Multi-Helix Bundles. *J. Am. Chem. Soc.* **2012,** *134*, 1606-1616.

75. Lanphere, C.; Offenbartl-Stiegert, D.; Dorey, A.; Pugh, G.; Georgiou, E.; Xing, Y.; Burns, J. R.; Howorka, S. Design, Assembly, and Characterization of Membrane-Spanning DNA Nanopores. *Nat. Protoc.* **2021,** *16*, 86-130.

76. Dertinger, T.; von der Hocht, I.; Loman, A.; Erdmann, R.; Enderlein, J. Latest Applications for 2-Focus Fluorescence Correlation Spectroscopy. *Proc. SPIE* **2008,** *6862*.

77. Armstrong, J. K.; Wenby, R. B.; Meiselman, H. J.; Fisher, T. C. The Hydrodynamic Radii of Macromolecules and Their Effect on Red Blood Cell Aggregation. *Biophys. J.* **2004,** *87*, 4259-4270.

78. Chenyakin, Y.; Ullmann, D. A.; Evoy, E.; Renbaum-Wolff, L.; Kamal, S.; Bertram, A. K. Diffusion Coefficients of Organic Molecules in Sucrose-Water Solutions and Comparison with Stokes-Einstein Predictions. *Atmos. Chem. Phys.* **2017,** *17*, 2423-2435.

79. Tonnesen, A.; Christensen, S. M.; Tkach, V.; Stamou, D. Geometrical Membrane Curvature as an Allosteric Regulator of Membrane Protein Structure and Function. *Biophys. J.* **2014,** *106*, 201-209.

80. Song, L.; Hobaugh, M. R.; Shustak, C.; Cheley, S.; Bayley, H.; Gouaux, J. E. Structure of Staphylococcal Alpha-Hemolysin, a Heptameric Transmembrane Pore. *Science* **1996,** *274*, 1859-1866.

81. Deen, W. M. Hindered Transport of Large Molecules in Liquid-Filled Pores. *AIChE J.* **1987,** *33*, 1409-1425.

82. Peters, R. Nucleo-Cytoplasmic Flux and Intracellular Mobility in Single Hepatocytes Measured by Fluorescence Microphotolysis. *EMBO J.* **1984,** *3*, 1831-1836.

83. Aksimentiev, A.; Schulten, K. Imaging Alpha-Hemolysin with Molecular Dynamics: Ionic Conductance, Osmotic Permeability, and the Electrostatic Potential Map. *Biophys. J.* **2005,** *88*, 3745-3761.

84. Lemkul, J. A.; Bevan, D. R. Assessing the Stability of Alzheimer's Amyloid Protofibrils Using Molecular Dynamics. *J. Phys. Chem. B* **2010,** *114*, 1652-1660.

85. Guros, N. B.; Balijepalli, A.; Klauda, J. B. The Role of Lipid Interactions in Simulations of the Alpha-Hemolysin Ion-Channel-Forming Toxin. *Biophys. J.* **2018,** *115*, 1720-1730.

86. *The Pymol Molecular Graphics System, Version 1.2r3pre*, Schrödinger, LLC.

87. Mackerell, A.; Vannomeslaeghe, K.; Gazula, V.; Chitre, B.; Puthanthodiyil, R.; Polani, N. K. *CGenFF Interface, Https://Cgenff.Umaryland.Edu* (accessed January 11, 2018).

88. Vanommeslaeghe, K.; Hatcher, E.; Acharya, C.; Kundu, S.; Zhong, S.; Shim, J.; Darian, E.; Guvench, O.; Lopes, P.; Vorobyov, I.; Mackerell, A. D., Jr. CHARMM General Force Field: A Force Field for Drug-Like Molecules Compatible with the Charmm All-Atom Additive Biological Force Fields. *J. Comput. Chem.* **2010,** *31*, 671-690.

89. Vanommeslaeghe, K.; MacKerell, A. D. Automation of the CHARMM General Force Field (CGenFF) I: Bond Perception and Atom Typing. *J. Chem. Inf. Model.* **2012,** *52*, 3144-3154.

90. Vanommeslaeghe, K.; Raman, E. P.; MacKerell, A. D., Jr. Automation of the Charmm General Force Field (CgenFF) II: Assignment of Bonded Parameters and Partial Atomic Charges. *J. Chem. Inf. Model.* **2012,** *52*, 3155-3168.

91. Abraham, M. J.; Murtola, T.; Schulz, R.; Pall, S.; Smith, J. C.; Hess, B.; Lindahl, E. Gromacs: High Performance Molecular Simulations through Multi-Level Parallelism from Laptops to Supercomputers. *SoftwareX* **2015,** *1-2*, 19-25.

92. Marrink, S. J.; de Vries, A. H.; Mark, A. E. Coarse Grained Model for Semiquantitative Lipid Simulations. *J. Phys. Chem. B* **2004,** *108*, 750-760.

93. Uusitalo, J. J.; Ingolfsson, H. I.; Akhshi, P.; Tieleman, D. P.; Marrink, S. J. Martini Coarse-Grained Force Field: Extension to DNA. *J. Chem. Theory Comput.* **2015,** *11*, 3932-3945.

94. Globisch, C.; Krishnamani, V.; Deserno, M.; Peter, C. Optimization of an Elastic Network Augmented Coarse Grained Model to Study Ccmv Capsid Deformation. *PLoS ONE* **2013,** *8*, e60582.

95. Wassenaar, T. A.; Ingolfsson, H. I.; Bockmann, R. A.; Tieleman, D. P.; Marrink, S. J. Computational Lipidomics with Insane: A Versatile Tool for Generating Custom Membranes for Molecular Simulations. *J. Chem. Theory Comput.* **2015,** *11*, 2144-2155.

96. Graham, J. A.; Essex, J. W.; Khalid, S. Pycgtool: Automated Generation of Coarse-Grained Molecular Dynamics Models from Atomistic Trajectories. *J. Chem. Inf. Model.* **2017,** *57*, 650–656.

97. Kumar, S.; Rosenberg, J. M.; Bouzida, D.; Swendsen, R. H.; Kollmann, P. A. The Weighted Histogram Analysis Method for Free-Energy Calculations on Biomolecules. I. The Method. *J. Comput. Chem.* **1992,** *13*, 1011-1021.